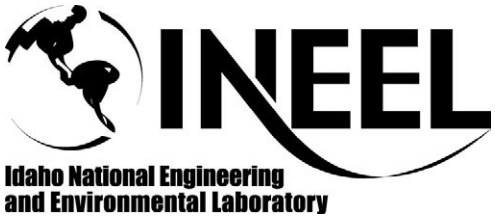

Idaho National Engineering
and Environmental Laboratory

INEEL/CON-99-01024
PREPRINT

Local Heat Transfer For Finned-Tube Heat Exchangers Using Oval Tubes

James E. O'Brien
Manohar S. Sohal

August 20, 2000

34th National Heat Transfer Conference

Proceedings of NHTC'00
34th National Heat Transfer Conference
Pittsburgh, Pennsylvania, August 20 – 22, 2000

NHTC2000-12093

LOCAL HEAT TRANSFER FOR FINNED-TUBE HEAT EXCHANGERS USING OVAL TUBES

James E. O'Brien, Manohar S. Sohal
Idaho National Engineering and Environmental Laboratory
Idaho Falls, ID 83415

Keywords: Heat transfer enhancement, horseshoe vortex, infrared imaging, oval tubes

ABSTRACT

This paper presents the results of an experimental study of forced convection heat transfer in a narrow rectangular duct fitted with either a circular tube or an elliptical tube in cross-flow. The duct was designed to simulate a single passage in a fin-tube heat exchanger. Heat transfer measurements were obtained using a transient technique in which a heated airflow is suddenly introduced to the test section. High-resolution local fin-surface temperature distributions were obtained at several times after initiation of the transient using an imaging infrared camera. Corresponding local fin-surface heat transfer coefficient distributions were then calculated from a locally applied one-dimensional semi-infinite inverse heat conduction model. Heat transfer results were obtained over an airflow rate ranging from 1.56×10^{-3} to 15.6×10^{-3} kg/s. These flow rates correspond to a duct-height Reynolds number range of 630 – 6300 with a duct height of 1.106 cm and a duct width-to-height ratio, W/H, of 11.25. The test cylinder was sized such that the diameter-to-duct height ratio, D/H is 5. The elliptical tube had an aspect ratio of 3:1 and a/H equal to 4.33. Results presented in this paper reveal visual and quantitative details of local fin-surface heat transfer distributions in the vicinity of circular and oval tubes and their relationship to the complex horseshoe vortex system that forms in the flow stagnation region. Fin surface stagnation-region Nusselt numbers are shown to be proportional to the square-root of Reynolds number.

INTRODUCTION

Air-cooled condensers used in binary-cycle geothermal power plants require the use of finned tubes in order to increase heat transfer surface area on the air side. Air is forced through several rows of these finned tubes by large fans. The condenser units can be very large, representing a large fraction of the overall capital cost of these plants. In addition, the power required to operate the fans represents a significant parasitic house load, reducing the net power production of the plant. The research presented in this paper has been undertaken with the aim of devising viable heat transfer enhancement strategies for application to geothermal air-cooled condensers and similar applications. An effective strategy can result in a reduction in condenser size and/or power consumption.

One heat transfer enhancement strategy that has been studied in some detail is the exploitation of longitudinal vortices to increase heat transfer coefficients with only small increases in pressure drop. These vortices are generated naturally in heat exchanger passages by the interaction of the flow with the heat exchanger tube. In this case, the vortices are called horseshoe vortices. Longitudinal vortices can also be created intentionally through the use of winglet vortex generators mounted or punched into the fin surfaces. Various winglet shapes have been used. An excellent review of heat transfer enhancement through the use of longitudinal vortices is given in [1].

A second heat transfer enhancement strategy which has received some recent attention is the usage of oval tubes instead of circular tubes in heat exchanger design [e.g., 2]. This strategy is not practical in all cases due to manufacturing considerations and the fact that circular tubes are inherently stronger and can therefore withstand much higher pressures with the same wall thickness. In any case, obvious advantages exist for oval tubes including reduced form drag and increased

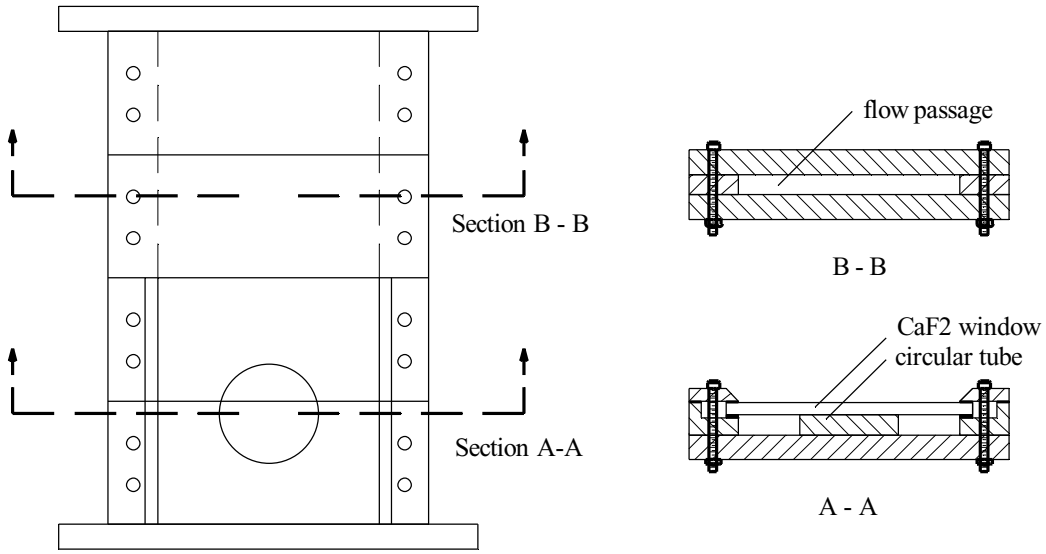

Figure 1. Test Section top view and cross-sections with circular tube.

tube-surface area for the same cross-sectional internal flow area.

A numerical studies of heat transfer enhancement with laminar flow in a finned oval tube with several rows of vortex generators on the fin surfaces are presented in [3, 4]. The results indicate that the winglets are responsible for significant heat transfer enhancement, as much as a factor of 3 on a local spanwise-average basis. This enhancement is accompanied by increased pressure losses, however.

In order to assess the heat transfer effectiveness of various combinations of tube and vortex-generator geometries, a heat transfer measurement technique that allows for high-resolution visualization and measurement of local heat transfer was chosen for this work. The focus of the work presented in this paper was to demonstrate the measurement technique and to document local heat transfer distributions for two baseline cases: single circular tube and single elliptical tube. During the next phase of the research, delta-winglet vortex generators will be placed in the test section in various single-tube configurations. The third phase will involve measurement of local heat transfer and pressure drop in single-channel, multiple-tube geometries with winglets. Finally, overall heat transfer and pressure drop will be measured for a multiple-channel, multiple-tube-row prototype heat exchanger.

NOMENCLATURE

a	elliptical tube major axis length, cm
b	elliptical tube minor axis length, cm
D	cylinder diameter, cm
h	heat transfer coefficient, W/m^2 K
H	channel height, cm
k	lexan thermal conductivity, W/m K
L	test section length, cm
$\dot{m}$	air mass flow rate, kg/s
$Nu_H = hH/k$	Nusselt number based on channel height
$Nu_D = hD/k$	Nusselt number based on cylinder diameter
R	cylinder radius, cm
$Re_H = \rho UH/\mu$	Reynolds number based on channel height
Re_D	Reynolds number based on cylinder diameter
t	time, s
T	temperature, K
T_i	initial temperature, K
T_∞	flow mean temperature, K
U	mean flow velocity, m/s
W	channel width, cm
x	cross-channel coordinate or semi-infinite solid depth coordinate, cm
α	lexan thermal diffusivity, m^2/s
$\gamma = \frac{h\sqrt{t}}{\sqrt{\rho ck}}$	nondimensional heat transfer coefficient
$\theta = \frac{T(0,t) - T_i}{T_\infty - T_i}$	nondimensional temperature difference
μ	air absolute viscosity, N s/m^2

APPARATUS

The experiments were performed in a narrow rectangular duct designed to simulate a single passage of a fin-tube heat exchanger. A drawing of the test section is shown in Fig. 1. Dimensions of the flow channel were W = 11.4 cm, H = 1.0 cm (4.5 in x 0.4 in). It is scaled up to approximately double-size compared to a typical fin-tube condenser heat exchanger.

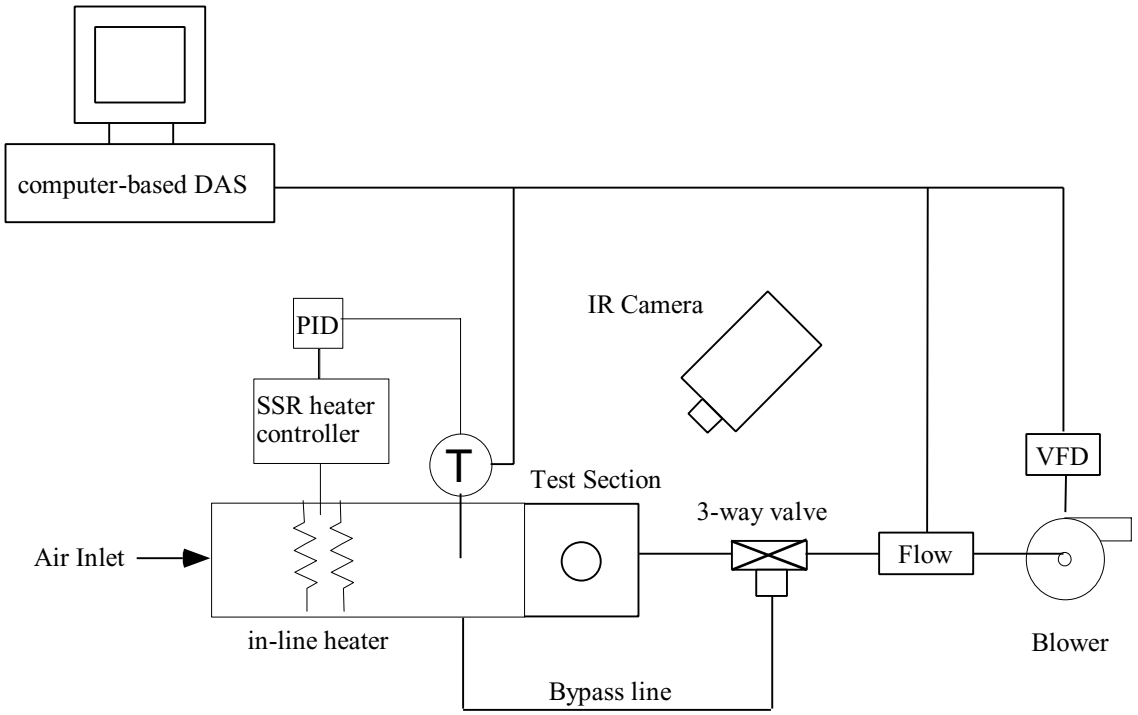

Figure 2. Schematic of experimental setup.

The duct was fabricated primarily out of lexan polycarbonate. For the first series of tests, a 5.08-cm (2.0 in) diameter circular disk, representing the circular tube of a fin-tube heat exchanger, also fabricated from lexan, was positioned in the center of the duct as shown. Additional tests were also performed with an elliptical-tube geometry. The elliptical tube was designed to have the same cross-sectional area as the circular tube and a 3:1 aspect ratio. The resulting minor and major axis lengths were 2b = 2.93 cm (1.15 in.) and 2a = 8.80 cm (3.464 in.), respectively. The test section length was 27.94 cm (11.0 in.), yielding L/H = 27.5. A flow development section with L/H = 30 was located upstream of the test section. Consequently, depending on Reynolds number, the flow is approximately hydrodynamically fully developed as it enters the test section.

In order to enable thermal visualization of the test section bottom surface (representing the fin surface), the top wall of the flow duct in the vicinity of the circular tube was made up of two calcium fluoride (CaF_2) windows, each 12.7 cm x 6.35 cm x 0.6 cm (5 in. x 2.5 in. x 0.24 in.). The test section bottom surface could therefore be viewed through the windows with an imaging infrared camera. Lexan is opaque in the sensitive wavelength range of the camera (3.6 to 5 μm). The transmissivity of the CaF_2 windows is very high (>95%) in this wavelength range. The test section bottom surface was painted black using ultra-flat black paint in order to achieve a surface emissivity very close to 1.0. This emissivity value was verified over a wide temperature range in separate camera calibration tests by comparing camera-indicated temperatures with surface temperatures measured using a precision thin-foil flush-mounted thermocouple bonded to a black-painted polycarbonate test surface. Therefore no emissivity corrections were required for the infrared temperature measurements.

A transient heat transfer measurement technique was employed for obtaining detailed local heat transfer measurements on the model fin surface. A schematic of the experimental setup is shown in Figure 2. Inlet air is heated to a desired setpoint temperature using an in-line feedback-controlled finned-element air heater (350 W). The heated air initially flows through a bypass line until the desired air temperature and flow rate is established. The air is then suddenly diverted through the test section by changing the position of a 3-way valve. Using this technique, the room-temperature fin/tube model is suddenly exposed to a uniformly heated airflow. Local surface temperatures on the model surfaces increase at a rate that is dependent on the value of the local heat transfer coefficient. This transient localized heating is quantitatively recorded using an imaging infrared camera. Values of local heat transfer coefficients can then be determined from an inverse heat conduction analysis.

The bypass flow is diverted from the main flow duct through a circular hole cut into the bottom of the flow development section. The center of the hole is located 8.25 cm (3.25 in.) upstream of the test section entrance. The duct walls downstream of this location are not preheated during the flow establishment period. Therefore this distance represents a thermal entry length. When flow is suddenly initiated through

the test section by changing the position of the 3-way valve, the flow bypass hole in the bottom of the flow development section is covered by sliding a flat lexan cover (sliding gate valve) over the hole. This procedure provides a continuous flat smooth flow surface, eliminating any concerns about a cavity-type flow disturbance associated with the hole.

Heater control is accomplished using a PID controller coupled to a solid-state relay with a pulsed relay output. A thermocouple mounted inside the duct measures the process variable. Air temperature uniformity across the duct was verified via infrared imaging of the test surface during preliminary tests with no test cylinder in place. Airflow rate is monitored through the use of a pitot probe mounted in the exhaust piping (3.81-cm schedule 40 PVC pipe). The probe tip is located in the center of the duct. The pressure differential generated by the pitot probe is measured using a precision variable-capacitance pressure transducer (MKS baratron model 223 B) with a 1-Torr range. Air is drawn through the system by a centrifugal blower (1/3 HP, 240 V 3-phase) located at the flow exit. Blower speed is controlled by a sub-micro inverter variable frequency drive (AC Tech model SF215), which in turn is controlled by a computer-generated 4-20 mA control signal. System flow rate varies linearly with blower speed over the range used in this study from about 1.56 x 10^{-3} kg/s (2.5 SCFM) at 460 rpm to 15.6 x 10^{-3} kg/s (25 SCFM) at 4600 rpm. These flow rates correspond to a duct-height Reynolds number ($Re_H = \rho UH/\mu = \dot{m}/\mu W$) range of 630 – 6300.

Two flush-mounted thin-foil thermocouples were bonded to the bottom surface of the test section near the test section inlet. These thermocouples provide a continuous indication of surface temperature at two locations and are used to help determine the exact start time of each test, which occurs when the heated airflow is diverted through the test section.

Quantitative thermal visualization images are obtained using a precision imaging infrared camera (FLIR PRISM DS). This camera uses a fully calibrated 320 x 244 platinum silicide IR CCD focal plane array detector which operates at a temperature of 77 K. The detector temperature is maintained by a mechanical split-stirling-cycle helium cryo-cooler. In its base mode of operation, the camera can be used to measure infra-red intensities corresponding to temperatures in the -10 to 250° C range, with extended ranges available through the use of filters up to 1500° C. The camera detector has a 12-bit digital dynamic range and a minimum discernible temperature difference (MDT) of 0.1° C at 30° C. It is equipped with a 25-mm standard lens, which provides a 17° x 13° field of view. All radiometric information is stored in binary digital files on PCMCIA flash memory cards for subsequent analysis. Infra-red thermography has several advantages over thermochromic liquid crystals for surface temperature mapping, including wide available temperature range, high spatial resolution, excellent thermal resolution, and full-field direct digital data acquisition and processing.

The thermal image data files created by the camera on-board processor are in a specialized 16-bit TIFF gray scale format (file extension .ana). These files include not only the image pixel values, but also a large amount of camera and test-specific information such as camera and firmware identifiers, date and time of image acquisition, camera settings at image acquisition, and temperature/pixel calibration data points. This information is included in the TIFF file in the form of "private tags" [5]. Specific file format information provided by FLIR was used in conjunction with general information about the TIFF standard found in reference [5] to fully decode the binary data files for subsequent thermal analysis using a Labview program created for this purpose.

Signals from all loop instrumentation were fed into a modular multiplexing data acquisition system (Hewlett Packard 3852A) which in turn was interfaced to a system-controller computer via an IEEE-488 bus. For this experiment, the data acquisition unit was configured with a 20-channel FET multiplexer with thermocouple compensation, a 5 1/2 digit integrating voltmeter, and a 4-channel voltage/current DAC. The DAC module was used to provide control signals (4-20 mA) to the variable-frequency blower drive. Data acquisition system programming was accomplished using Labview (National Instruments Version 5.1) software. The data files included time histories of the thermocouple and pressure-transducer signals with updates at 0.7 second intervals.

EXPERIMENTAL PROCEDURE

As mentioned previously, a transient heat transfer technique was employed in order to obtain measurements of local heat transfer coefficients on model fin surfaces. Details of the experimental procedure will now be provided. After the IR camera is powered up and the detector array has reached its operating temperature, the camera is positioned above the test section at an appropriate height for observing either the entire portion of the test section or a close-up view. In order to avoid IR reflections of the warm camera body off the CaF_2 windows, the camera is positioned at a small angle off the vertical. The camera gain and level adjustments are set such that the minimum observable temperature corresponds to the initial temperature with a temperature range of 10 – 15° C. The software clock on the camera is synchronized with the clock on the data acquisition computer to within ±0.5 s. The 3-way valve is set to the bypass position and the sliding gate valve is opened. Flow is initiated through the bypass line by adjusting the blower RPM until the desired flow rate is observed. The air temperature is established by adjusting the

PID controller set point value to the desired level, typically 45° C. Before diverting heated air through the test section, a pre-test thermal image of the test section is acquired. At this time, the data acquisition system is set to begin writing data to disk. The 3-way valve position is then changed and the sliding gate valve is closed to divert the heated airflow through the test section, initiating the convective thermal transient. A number of thermal images of the test section (typically 5) are acquired during the first 5 – 60 seconds of the transient. These images are stored on PCMCIA flash memory cards and are transferred to the system controller computer after each test.

DATA REDUCTION

The objective of the tests is to obtain detailed maps of local heat transfer coefficient. The IR images provide local surface temperatures at specified times after initiation of the transient. In order to obtain heat transfer coefficients from the measured surface temperatures, the bottom surface of the test section is assumed to behave locally as a one-dimensional semi-infinite solid undergoing a step change in surface heat transfer coefficient. For the 1.27-cm thickness of the lexan test surface, the semi-infinite assumption is valid for at least 88 seconds after initiation of the transient. The time-dependent one-dimensional temperature field within a semi-infinite solid subjected to this boundary condition is given by [6]:

$$\frac{T(0,t)-T_i}{T_\infty - T_i} = erfc\left(\frac{x}{2\sqrt{\alpha t}}\right) - \left[\exp\left(\frac{hx}{k}+\frac{h^2\alpha t}{k^2}\right)\right]\left[erfc\left(\frac{x}{2\sqrt{\alpha t}}+\frac{h\sqrt{\alpha t}}{k}\right)\right] \quad (1)$$

The time-dependent surface (x = 0) temperature is therefore given by:

$$\frac{T(0,t)-T_i}{T_\infty - T_i} = 1 - \exp\left(\frac{h^2\alpha t}{k^2}\right) erfc\left(\frac{h\sqrt{\alpha t}}{k}\right) \quad (2)$$

and if we let

$$\theta = \frac{T(0,t)-T_i}{T_\infty - T_i} \; ; \; \gamma = \frac{h\sqrt{\alpha t}}{k} = \frac{h\sqrt{t}}{\sqrt{\rho c k}} \quad (3)$$

the equation reduces to

$$\theta = 1 - \exp(\gamma^2) erfc(\gamma) \quad (4)$$

This equation represents the relationship between heat transfer coefficient and surface temperature measured at a specific time after the start of the test. It must be solved iteratively for γ.

However, since the camera pixel array includes over 78000 pixels, it is not practical to directly solve the equation at every pixel. Instead, a look-up table approach was used in the data reduction scheme. The measured temperature range for each thermal image is divided into 100 increments and a value of heat transfer coefficient is obtained for each of these 100 temperatures by iteratively solving equation (4). Each actual pixel temperature is then converted to a heat transfer coefficient by linear interpolation among the 100 increments.

RESULTS

This study will be performed in several phases. The initial phase, which is the subject of this paper, is focused on measurement of local heat transfer coefficient distributions in two baseline configurations: single circular tube and single oval tube. In phase 2, local heat transfer will be measured with winglet vortex generators in various configurations added to the single-tube geometries. Phase 3 will involve measurement of local heat transfer and pressure drop in single-channel, multiple-tube geometries with winglets. Overall heat transfer and pressure drop will be measured for a multiple-channel, multiple tube-row prototype heat exchanger during Phase 4.

The first baseline configuration studied was a single circular tube. Local fin-surface heat transfer results for this configuration are presented in Figs. 3 – 7. Heat transfer results are presented as a function of Reynolds number based on channel height, H. Heat transfer coefficients are based on

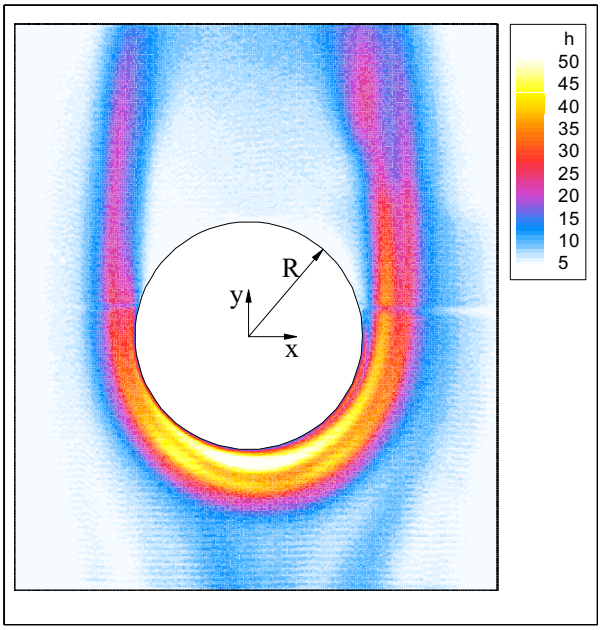

Figure 3. Color contour map of local heat transfer coefficient, h (W/m^2 K), circular cylinder, Re_H = 1000.

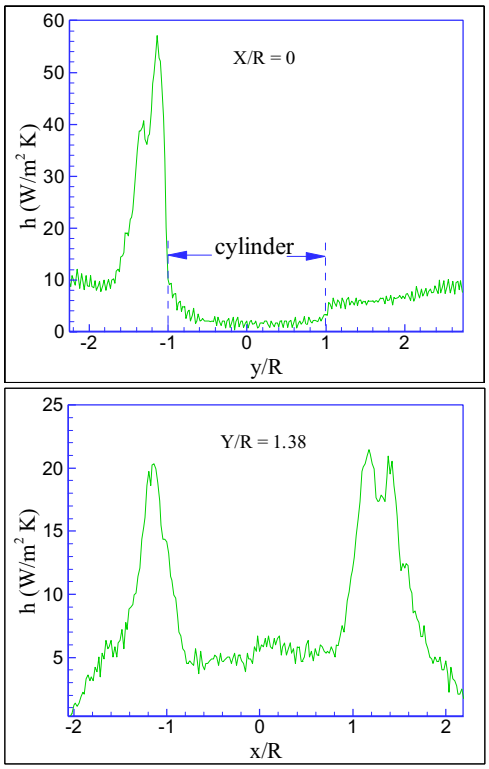

Figure 4. Top: centerline variation of heat transfer coefficient; bottom: transverse variation of heat transfer coefficient in wake region.

the test section inlet temperature. A color contour map of local heat transfer coefficient for $Re_H = 1000$ is presented in Fig. 3. The figure reveals several interesting features including the heat transfer signature of the horseshoe vortex system that forms in the forward stagnation region around the base of the cylinder and is swept downstream as longitudinal vortices. Heat transfer coefficients on the fin surface in the forward stagnation region are approximately a factor of 10 higher than corresponding fully developed duct values. A double peak in local heat transfer is evident in the forward stagnation region. This double peak has been observed in several previous studies [e.g., 7-9] using both mass transfer analogy techniques and liquid crystal thermography. The double peak is associated with the complex multiple-vortex structure that becomes established in the forward stagnation region at the base of a bluff object such as a circular cylinder when a laminar boundary layer flow encounters the object. A detailed study of the fluid mechanics of laminar horseshoe vortices is presented in reference [10]. Figure 3 indicates that flow separation occurs at approximately 90 degrees from the forward stagnation line, which is characteristic of laminar flow separation. The wake region is quite large at this Reynolds number and heat transfer coefficients in the wake region are very low. The coordinate system used in subsequent figures is indicated in Figure 3 with the origin located at the center of the cylinder.

Two line plots of local heat transfer coefficient obtained from Fig. 3 are presented in Fig. 4. The top plot represents the variation in local heat transfer along the duct centerline at x/R=0. The double peak in heat transfer coefficient in the forward stagnation region can also be seen in this figure. Heat transfer coefficients are very high in the forward stagnation region, peaking at around 58 W/m^2 K. Upstream of the stagnation region, h values are near 10 W/m^2 K. Wake region values are closer to 5 W/m^2 K.

A cross-plot of the transverse variation of local heat transfer

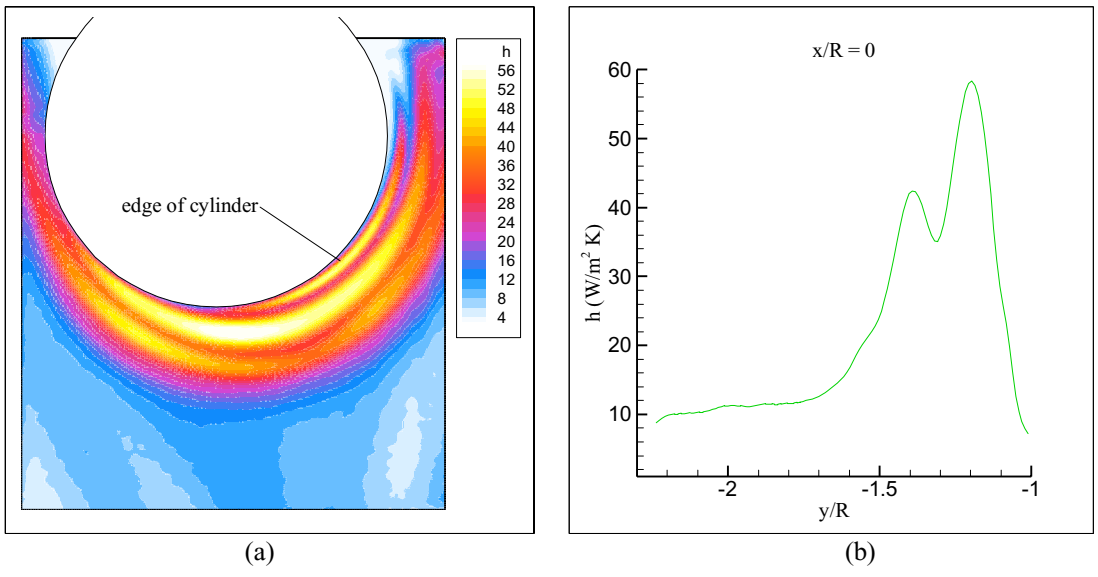

Figure 5. Cylinder stagnation region details, ReH = 1080; (a) contour plot, (b) centerline h

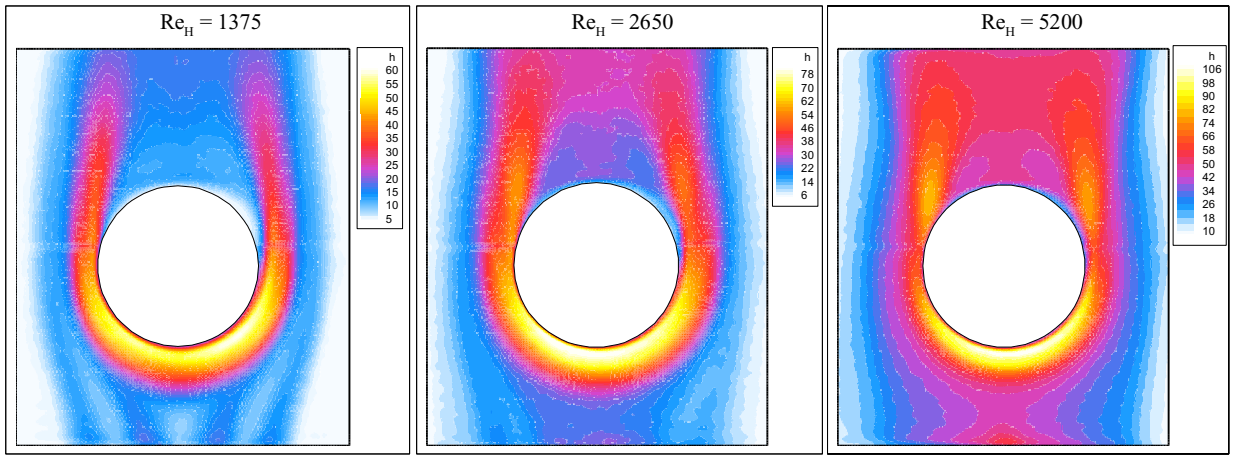

Figure 6. Heat transfer distribution trends with Reynolds number, circular tube.

coefficient obtained from Fig. 3 is presented in the lower plot of Fig. 4. This figure reveals the variation in local heat transfer coefficient across the duct span at a fixed value of y/R = 1.38. Two major peaks associated with the horseshoe vortex system are evident. The rightmost of these peaks has two sub-peaks, remnants of the multiple-vortex structure of the horseshoe vortex.

A close-up of the cylinder stagnation region at Re_H = 1080 is presented in Fig. 5 along with a plot of the centerline variation of heat transfer coefficient. In order to avoid capturing reflection of the camera itself off the CaF windows, the thermal images are acquired with the camera positioned at a small angle off the vertical. Therefore, the edge of the test cylinder can be seen in the image, as indicated in Fig. 5. The close-up heat transfer contour plot again clearly shows the double peak in heat transfer in the forward stagnation region. A higher resolution line plot of the centerline variation in heat transfer coefficient in the forward stagnation region is shown in the right portion of Fig. 5.

Heat transfer distributions at three additional Reynolds numbers are presented in Fig. 6. At Re_H = 1375, the duct flow is laminar and flow separation occurs near 90º. The approach flow at this Reynolds number is characterized by four distinct longitudinal streaks which are deflected around the cylinder. A hint of similar streaks is also visible at Re_H = 1000 (Fig. 4) and in Fig. 6 at Re_H = 2650, but they are by far the most evident at Re_H = 1375. These streaks may be caused by secondary flows that become established in the rectangular-

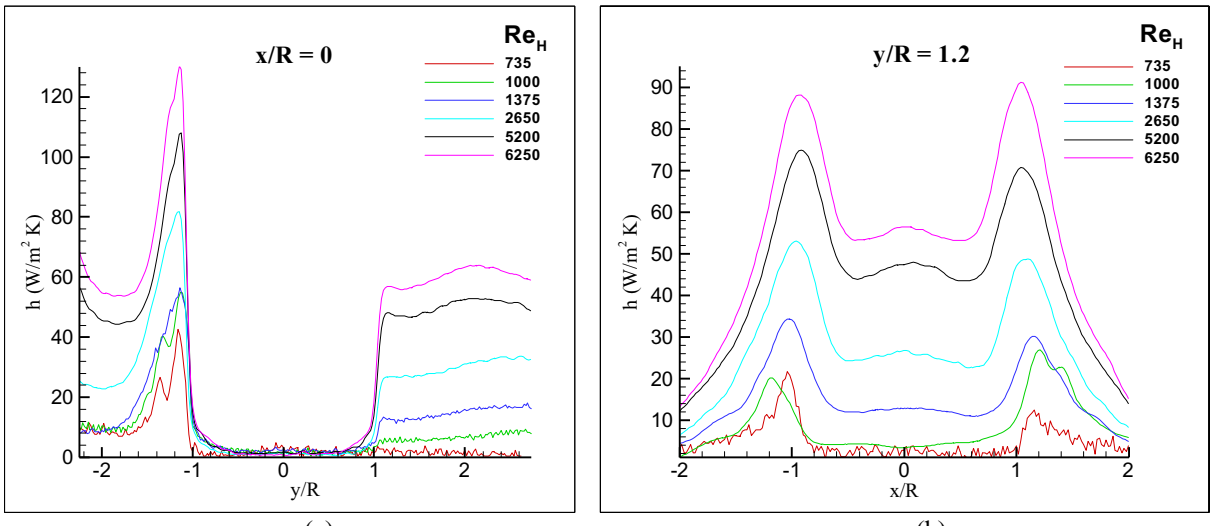

Figure 7. Line plots of fin-surface heat transfer coefficient, circular tube; (a) streamwise variation along duct centerline, (b) wake region transverse variation, y/R = 1.20.

duct flow development section. At $Re_H = 1375$, the horseshoe vortices downstream of the cylinder begin to bend inward toward the wake region. At $Re_H = 2650$, flow separation is delayed to around 110º from the stagnation line and the wake region begins to "fill in" with relatively high heat transfer coefficients due to increased turbulent mixing. This trend continues at ReH = 5200 with a much larger region of high heat transfer coefficients. It should be noted that many commercial heat exchangers including geothermal air-cooled condensers operate at Re_H values below 1000. At low Reynolds numbers, the regions of increased heat transfer are constrained to relatively small regions just upstream and to the sides of the tube and in the immediate vicinity of the horseshoe vortices downstream of the tube. Therefore, at low Reynolds numbers, there is great potential for significant heat transfer enhancement through the usage of strategically placed vortex generators on fin surfaces.

Line plots of local fin-surface heat transfer coefficient trends with Reynolds number are presented in Fig. 7. Fig. 7(a) represents duct-centerline heat transfer coefficients along x/R = 0 and Fig. 7(b) represents the transverse variation in heat transfer coefficient in the wake region at y/R = 1.2. The large peak in heat transfer coefficient in Fig. 7(a) at y/R ~ -1.3 is associated with the forward stagnation region horseshoe vortex. Heat transfer coefficients in the wake region (y/R>1) are very close to zero for the lowest Reynolds number shown and increase dramatically with increasing Reynolds number. The two peaks seen in Fig. 7(b) at each Reynolds number result from the downstream longitudinal portion of the horseshoe vortex. Examination of these figures reinforces the fact that heat transfer coefficients increase with Reynolds number and are more uniform at higher Reynolds numbers due to turbulent mixing. At low Reynolds numbers, relatively high heat transfer coefficients are confined to very small areas in the stagnation and horseshoe vortex regions.

A series of contour plots of local heat transfer coefficient in the vicinity of an elliptical tube is presented in Fig. 8 for four Reynolds numbers. The elliptic tube was fabricated with the same cross-sectional area as the circular tube used in the previous tests. It had a 3:1 aspect ratio between the major and minor axis lengths. The distributions appear to be slightly asymmetric. This asymmetry is due to the IR-camera viewing angle, as indicated previously in the discussion of Fig. 5. These contour plots exhibit trends that are similar to the circular-tube heat transfer distributions presented in Fig. 6. At the lowest Reynolds number shown, $Re_H = 1410$, longitudinal streaks are evident, similar to the streaks seen in Fig. 6 at $Re_H = 1375$. These streaks do not appear to be directly related to the horseshoe vortex system, but rather may be formed as secondary flows in the rectangular flow-development duct well upstream of the elliptical tube. The streaks are again most obvious only at one of the Reynolds numbers shown, $Re_H = 1410$. They can also be seen at $Re_H = 2800$, but not as distinctly. As in the circular-tube cases, a horseshoe vortex system is also established for the elliptical tube cases. It results in the high stagnation-region heat transfer coefficients seen in Fig. 8. In addition, longitudinal vortices are produced and swept downstream of the stagnation region, resulting in enhanced heat transfer along the sides and downstream of the elliptical tube. The heat transfer results indicate that the flow separation point moves downstream and that the size of the low-heat-transfer wake region shrinks significantly with increasing Reynolds number.

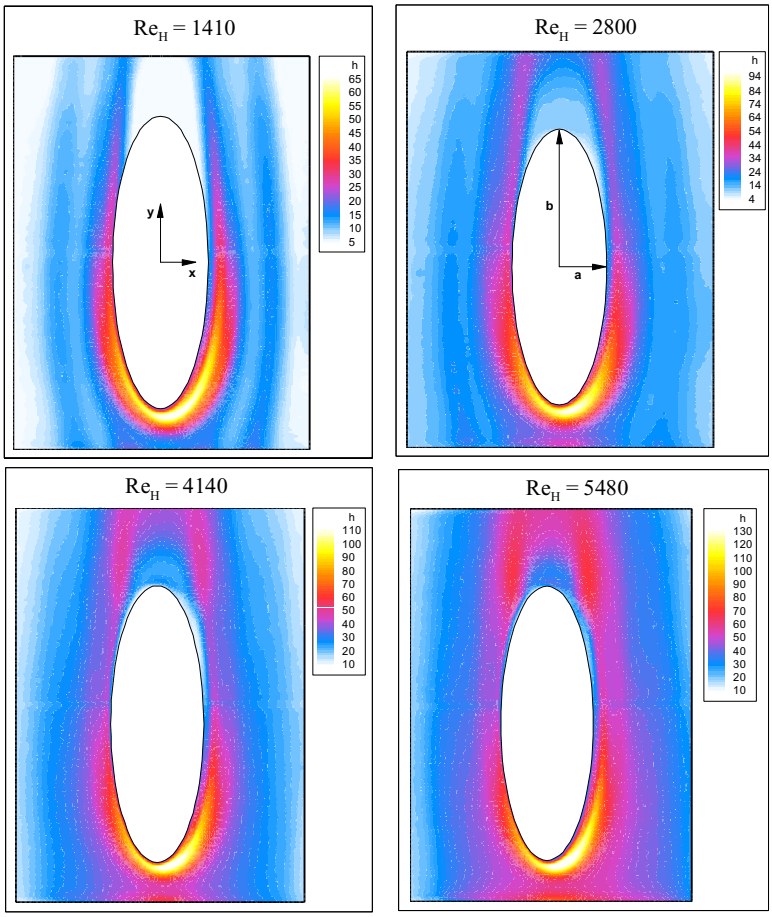

Figure 8. Local heat transfer coefficients surrounding an elliptical tube, four Reynolds numbers.

Line plots of local fin-surface heat transfer coefficients along the duct centerline in the forward stagnation region of the elliptical tube are presented in Fig. 9(a) for the four Reynolds numbers presented in Fig. 8. The transverse variation of local fin-surface heat transfer coefficient in the elliptical-tube wake

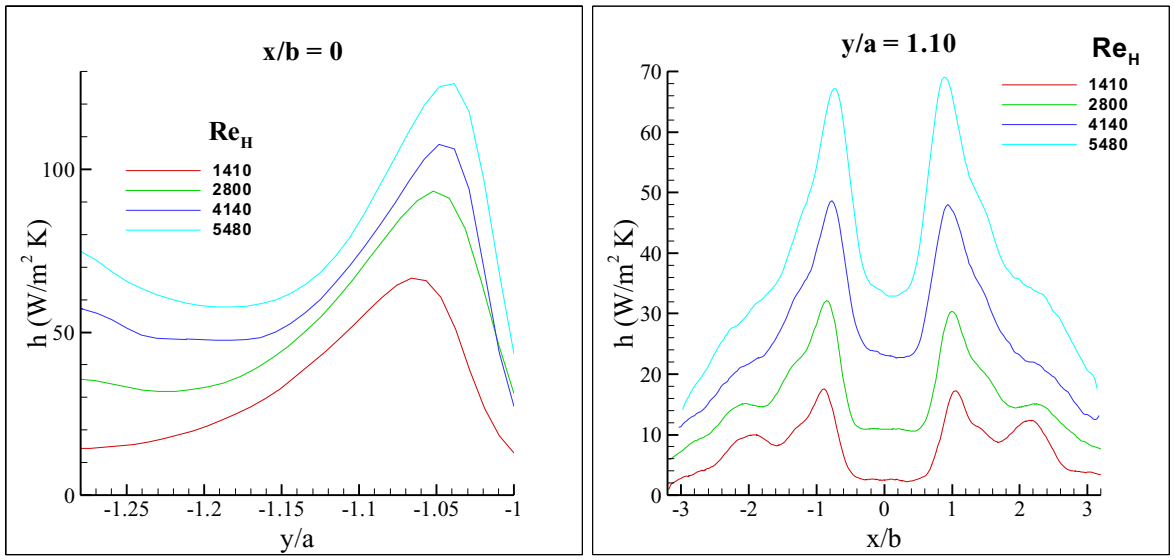

Figure 9. Line plots of fin-surface heat transfer coefficient, elliptical tube; (a) stagnation-region streamwise variation along duct centerline, (b) wake region transverse variation, y/a = 1.10.

region is presented in Fig. 9(b). Stagnation region heat transfer coefficients are similar in shape and magnitude to the corresponding values for the circular tube. The shapes of the wake region transverse variation in heat transfer coefficient plots (Fig 9b) again reveal two peaks associated with the horseshoe vortices shed from the elliptical tube. There is an additional local maximum in heat transfer coefficient visible at the two lowest Reynolds numbers associated with the longitudinal streaks visible in Fig. 8.

Maximum stagnation-region heat transfer coefficients have been obtained from the circular-tube and elliptical-tube data and cast in terms of Nusselt numbers based on channel height, Nu_H. These Nusselt numbers are presented in Fig. 10 as a function of Reynolds number based on channel height, Re_H, along with power-law curve fits with the exponent on Re_H forced to be 1/2. The resulting correlations for the two geometries are shown in the figure. The maximum Nusselt number data are well fitted by Frössling-type [11] correlations, as shown. This result indicates that the heat transfer process in the stagnation region near the fin surface is dominated by laminar energy transport, even at Reynolds numbers that produce turbulent flow in the duct. Therefore for the tube and duct geometries studied, the fin surface in the stagnation region behaves similarly to the tube surface near its stagnation line. If the circular cylinder correlation is recast using tube diameter as the characteristic dimension for both Reynolds number and Nusselt number, it becomes:

$$Nu_D = 1.43\, Re_D^{1/2} \qquad (5)$$

Nusselt numbers on the stagnation-line of an infinite circular cylinder in a low-turbulence cross-flow would be better predicted using a Reynolds-number coefficient close to 1.0. For a cylinder mounted in a channel flow, however, this coefficient has been shown to be higher. Examination of the fin-surface data presented in reference [2] from a fin/tube geometry, generated through the use of an ammonia-absorption mass-transfer-analogy technique, and converted to

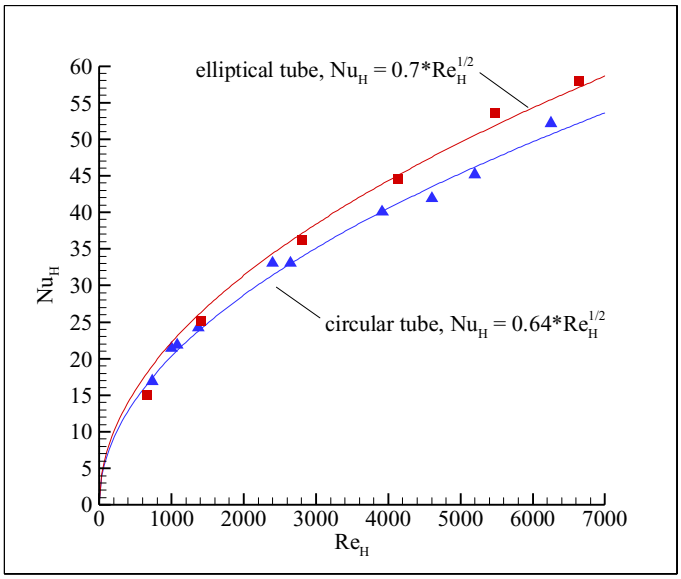

Figure 10. Maximum fin-surface Nusselt numbers with correlations.

heat transfer results using the heat/mass transfer analogy produces a coefficient of 1.41 for equation (5).

SUMMARY AND CONCLUSIONS

An experimental study of local heat transfer in a narrow rectangular duct fitted with either a circular tube or an elliptical tube in cross-flow has been performed. The duct was designed to simulate a single passage in a fin-tube heat exchanger with a duct height of 1.106 cm and a duct width-to-height ratio, W/H, of 11.25. The test section length yielded L/H = 27.5 with a flow development length of L/H = 30. The test cylinder was sized to provide a diameter-to-duct height ratio, D/H of 5. The elliptical tube had an aspect ratio of 3:1 and a/H equal to 4.33.

Heat transfer measurements were obtained using a transient technique in which a heated airflow was suddenly introduced to the ambient-temperature test section. High-resolution local test-surface temperature distributions were obtained at several times after initiation of the transient using an imaging infrared camera. Corresponding local fin-surface heat transfer coefficient distributions were calculated from a locally applied one-dimensional semi-infinite inverse heat conduction model. Heat transfer results were obtained over an airflow rate ranging from 1.56×10^{-3} to 15.6×10^{-3} kg/s. These flow rates correspond to a duct-height Reynolds number range of 630 – 6300.

The transient heat transfer measurement technique used in this study has been shown to produce excellent high-resolution local heat transfer results. Results presented in this paper for the circular cylinder case agree very well with literature sources. Details of the complex horseshoe vortex region system are revealed in the local heat transfer results. Low Reynolds number heat transfer measurements indicate a double peak in local fin-surface heat transfer in the stagnation region. At low Reynolds numbers, regions of relatively high heat transfer are constrained to small regions just upstream and to the sides of the tube and in the immediate vicinity of the horseshoe vortices downstream of the tube. Therefore, at low Reynolds numbers, there is great potential for significant heat transfer enhancement through the usage of strategically placed vortex generators on fin surfaces. Heat transfer distributions are much more uniform at high Reynolds number due to increased turbulent mixing. Oval tube heat transfer results indicate a similar horseshoe vortex system as is produced with circular tubes. Heat transfer distribution results indicate that the flow separation point moves downstream and that the size of the low-heat-transfer wake region shrinks significantly with increasing Reynolds number. Maximum stagnation region heat transfer results for both circular and elliptical tubes correlate well with a square-root of Reynolds number dependency, indicating that the heat transfer process in the stagnation region near the fin surface is dominated by laminar energy transport, even at Reynolds numbers that produce turbulent flow in the duct.

ACKNOWLEDGMENTS

This work was sponsored by the U.S. Department of Energy, Geothermal Program. The Idaho National Engineering and Environmental Laboratory is operated by Bechtel, Babcock and Wilcox Idaho, LLC under contract number DE-AC07-99ID13727.

REFERENCES

1. Jacobi, A. M., and Shah, R. K., "Heat Transfer Surface Enhancement through the Use of Longitudinal Vortices: A Review of Recent Progress," *Experimental Thermal and Fluid Science*, Vol. 11, pp. 295-309, 1995.
2. Chen, Y., Fiebig, M., and Mitra, N. K., "Conjugate Heat Transfer of a Finned Oval Tube Part B: Heat Transfer Behaviors," *Numerical Heat Transfer*, Part A, Vol. 33, pp. 387-401, 1998.
3. Chen, Y., Fiebig, M., and Mitra, N. K., "Heat Transfer Enhancement of a Finned Oval Tube with Punched Longitudinal Vortex Generators In-line," Intl. Journal of Heat and Mass Transfer, Vol. 41, pp. 4151-4166, 1998.
4. Chen, Y., Fiebig, M., and Mitra, N. K., "Conjugate Heat Transfer of a Finned Oval Tube with a Punched Longitudinal Vortex Generator in Form of a Delta-winglet – Parametric Investigations of the Winglet," Intl. Journal of Heat and Mass Transfer, Vol. 41, pp. 3961-3978, 1998.
5. Carlsen, S., "TIFF revision 6.0," Aldus Developers Desk (http://icib.igd.fhg.de/icib/it/defacto/company/aldus/read.html#SEC_2), Aldus Corporation, 1992.
6. Incropera, F. P., and DeWitt, D. P., *Fundamentals of Heat and Mass Transfer*, 3rd edition, John Wiley and Sons, New York, 1990.
7. Krückels, W., and Kottke, V., "Untersuchung über die Verteilung des Wärmeübergangs an Rippen und Rippenrohr-Modellen," *Chemie Ingenieur Technik*, Vol. 42, No. 6, pp. 355–362, 1970.
8. Goldstein, R. J., and Karni, J., "The Effect of a Wall Boundary Layer on Local Mass Transfer from a Cylinder in Crossflow," *Journal of Heat Transfer*, Vol. 106, pp. 260-267, 1984.
9. Ireland, P. T., and Jones, T. V., "Detailed Measurements of Heat Transfer on and around a Pedestal in Fully Developed Passage Flow," Proceedings, 8th Intl. Heat Transfer Conference, Vol. 3, pp. 975-980, San Francisco, 1986.
10. Baker, C. J., "The Laminar Horseshoe Vortex," *Journal of Fluid Mechanics*, Vol. 95, part 2, pp. 347-367, 1979.
11. Frössling, N., "Evaporation, Heat Transfer, and Velocity Distribution in Two-Dimensional and Rotationally Symmetric Laminar Boundary Layer Flow," NACA TM-1432, 1958.

